actuators

MDPI

Article

Integration of Shape Memory Alloy Actuators into Sintered Aluminum Structures via Material Extrusion for Aerospace Applications

Bernardo Alves [1,†], Rafael Sousa [1,†], Ricardo Coelho [1], Gonçalo Oliveira [1], Luís Cacho [1], Daniel Gatões [1], Rodolfo Teixeira [2] and Patrícia Freitas Rodrigues [1,*]

[1] ARISE/CEMMPRE, Department of Mechanical Engineering, University of Coimbra, Rua Lus Reis Santos, 3030-788 Coimbra, Portugal; bernardo.alves@uc.pt (B.A.); uc2020233770@student.uc.pt (R.S.); luis.cacho@dem.uc.pt (L.C.); daniel.gatoes@uc.pt (D.G.)

[2] School of Mechanical Engineering, University of Campinas, Campinas 13083-860, SP, Brazil; rst@unicamp.br

* Correspondence: pf.rodrigues@uc.pt

† These authors contributed equally to this work.

Abstract

Reducing structural mass and volume is critical to improving efficiency and payload capacity in next-generation small satellites and CubeSats. Additive manufacturing, particularly material extrusion, offers design flexibility and enables the production of lightweight, functional metallic components. This study investigates the integration of nickel–titanium shape memory alloy wires into aluminum-based matrices using a sinter-based material extrusion process, aiming to develop compact actuator systems for aerospace applications. A customized AlSi7Mg aluminum alloy feedstock was extruded into filament form, printed, and embedded with shape memory alloy wires, allowing consolidation during sintering. X-ray micro-computed tomography was used to analyze internal defects and matrix–wire interfacial contact, before and after sintering. Tensile testing of the embedded actuator structures revealed effective mechanical bonding and actuation behavior. The results demonstrate that controlled shrinkage and interfacial bonding enable reliable embedding of shape memory elements without compromising structural integrity. This work provides a promising framework for developing multifunctional aerospace components, where active actuation and structural efficiency can be combined through advanced material extrusion-based manufacturing.

Keywords: material extrusion; shape memory alloy; NiTi actuator integration; aluminum Sintering; aerospace structures

check for updates

Academic Editors: Todor Stoilov Todorov, Rosen Mitrev and Wei Min Huang

Received: 15 May 2025
Revised: 16 June 2025
Accepted: 19 June 2025
Published: 21 June 2025

Citation: Alves, B.; Sousa, R.; Coelho, R.; Oliveira, G.; Cacho, L.; Gatões, D.; Teixeira, R.; Freitas Rodrigues, P. Integration of Shape Memory Alloy Actuators into Sintered Aluminum Structures via Material Extrusion for Aerospace Applications. *Actuators* **2025**, *14*, 305. https://doi.org/10.3390/act14070305

Copyright: © 2025 by the authors. Licensee MDPI, Basel, Switzerland. This article is an open access article distributed under the terms and conditions of the Creative Commons Attribution (CC BY) license (https://creativecommons.org/licenses/by/4.0/).

1. Introduction

The demand for reduced mass and volume remains central to the design of modern aerospace systems, especially in small satellites and CubeSats, where launch cost, structural stability, and payload efficiency are tightly coupled to weight constraints. Minimizing structural mass enables higher payload-to-weight ratios and increases mission versatility within limited launch envelopes [1]. Recent structural studies have shown that using multifunctional composite designs in CubeSats can enhance volumetric efficiency by up to 37% and reduce structural mass fractions to as low as 16.7%, significantly improving system performance [2]. Additionally, new retractable truss-based CubeSat configurations have demonstrated compact stowage, reliable deployment, and enhanced payload accommodation, while maintaining structural rigidity [3].

To address the mass and geometric constraints inherent to small satellite platforms, additive manufacturing (AM) has emerged as a transformative approach for producing lightweight, complex aerospace structures with minimal material waste. Among AM techniques, material extrusion (MEX), a process that extrudes thermoplastic filaments filled with metallic powders, has attracted attention due to its cost-effectiveness, safety, and design flexibility. In this method, shaped "green parts" are subsequently subjected to debinding and sintering to produce dense metallic components suitable for structural use [4–7]. MEX is particularly valuable for low-volume aerospace applications, where rapid prototyping, functional integration, and cost constraints are critical [1]. Recent advances have shown that MEX can yield sintered components with relative densities above 97%, bridging the gap between prototyping and functional end-use parts [8]. Additionally, Singh et al. demonstrated that metal injection molding (MIM) feedstock adapted for extrusion can be successfully processed using multi-step debinding and sintering to obtain densities approaching 95.6%, confirming the viability of MEX for high-performance applications [9].

The quality of the final part is strongly influenced by feedstock composition, extrusion parameters, and the sintering cycle. Studies using stainless steel powders have shown that feedstock formulation and thermal profile optimization are critical to reduce porosity, control shrinkage, and preserve dimensional accuracy, requirements essential for aerospace-grade components [4].

One such functional element is the shape memory alloy (SMA), particularly nickel–titanium (NiTi), which is widely used for its shape recovery capability, superelasticity, and high energy-to-weight ratio. These properties originate from a reversible thermoelastic martensitic transformation between the austenite and martensite phases. This transformation can be triggered either thermally or via Joule heating, enabling compact, efficient actuation with significant force and displacement [10,11].

Recent studies have confirmed the suitability of NiTi for aerospace actuators under cyclic thermal and mechanical loads. Zhao et al. (2019) demonstrated that NiTi wires under thermo-mechanical cyclic loading exhibit gradual strain accumulation and reduced energy dissipation, but maintain predictable actuation characteristics over multiple cycles, a key factor for aerospace reliability [12]. In a complementary study, Liu et al. (2024) showed that aged NiTi samples achieved over 90% recovery rate after 10 actuation cycles under Joule-induced phase transformation, validating their use in repetitive aerospace mechanisms [13,14].

NiTi actuators offer distinct advantages for aerospace systems, including silent operation, compact form factor, low power consumption, and high energy-to-weight ratios. These characteristics make SMAs especially suitable for deployable mechanisms in space, such as solar panels and antennas. Their activation via Joule heating simplifies the control system and reduces mechanical complexity, which is critical for volume-constrained platforms like CubeSats.

Regarding nanosatellites, the need for autonomous deployment mechanisms has pushed forward the demonstration of the effectiveness of SMA-based systems for CubeSats. For instance, Carnier (2023) developed a torsion-based NiTi actuator integrated into the thermal circuit of a CubeSat to passively deploy a radiator panel using only waste heat from internal fluid circulation. The system demonstrated reliable deployment triggered via the shape memory effect and validated the feasibility of power-efficient actuation using internal thermal energy [15]. Boschetto et al. (2019) developed and tested self-deploying solar sails actuated by NiTi wires, demonstrating functional prototypes with high planarity and repeatable performance, validating SMA integration for lightweight autonomous deployment in orbital systems [16].

The integration of NiTi shape memory actuators into metallic structures, especially aluminum-based matrices like AlSi7Mg, presents significant engineering challenges. Differences in thermal expansion coefficients, poor interfacial bonding, and the formation of oxides or intermetallic compounds during processing can impair both structural integrity and actuation functionality. Moreover, conventional manufacturing techniques offer limited control over the geometric and compositional fidelity required for functional SMAs, due to poor machinability and high reactivity. These factors can lead to localized defects, residual stresses, and phase transformation shifts that critically affect NiTi performance.

Huang et al. (2019) demonstrated that a well-bonded interface between NiTi particles and an aluminum matrix could still experience mechanical degradation due to residual stress and phase mismatch, although underwater friction stir processing helped limit intermetallic formation and preserved shape memory behavior [17]. Similarly, Tang et al. used numerical simulation to show that NiTi/Al composites develop significant residual stresses during cooling cycles due to the thermal expansion mismatch, which can impact phase stability and fatigue life [18].

Therefore, this study proposes to investigate and optimize the integration of NiTi SMA into aluminum-based structures produced via MEX, a sinter-based AM route. The aim is to enable the development of lightweight, multifunctional components specifically designed for aerospace applications where mass reduction and system simplification are critical. This research emphasizes the integration of a spring (actuator) before the sintering process, effectively embedding the actuator on the metallic matrix, and the subsequent analysis of bonding quality, defect evaluation, and mechanical integrity at the wire–matrix interface. To achieve this, advanced non-destructive and mechanical characterization techniques are applied, including X-ray microtomography, to assess pore networks and embedding fidelity, and tensile testing to quantify interfacial strength and actuation compatibility. By validating the embedding approach through structural and functional performance metrics, this study provides a foundation for the use of MEX-production smart structures in deployable CubeSat mechanisms, adaptive surfaces, and several aerospace systems.

Following this introduction, Section 2 presents the materials and methods used in this study. Section 3 reports and discusses the experimental results. Finally, Section 4 outlines the main conclusions and potential applications.

2. Materials and Methods

This study followed a four-stage methodology: (i) filament preparation from AlSi7Mg powder, (ii) printing of green parts with embedded shape memory alloy wires, (iii) sintering under controlled conditions, and (iv) post-sintering characterization, including μCT analysis, tensile testing, and actuation cycling.

2.1. Materials

2.1.1. Feedstock Materials

The metallic feedstock was formulated using a gas-atomized AlSi7Mg (EN ISO 18273, purchased from Carpenter Additive, Philadelphia, PA, USA) aluminum alloy powder. The powder had a particle size distribution (D_{50}) of 45 μm, with a near-spherical morphology to promote flowability. The binder system consisted of a multicomponent polymer blend (purchased from Emery Oleochemicals, Cincinnati, Ohio, USA) optimized for filament extrusion, composed of polyamide copolymers, ester wax, and stearic acid (SA). This combination was selected to provide a low melting point and flowability, powder dispersion, and reduced viscosity. All binder components were sourced as commercial-grade materials and used without further purification.

2.1.2. NiTi Spring

The NiTi shape memory alloy (SMA) tensile springs (purchased from SAES Group—Tensile Spring) exhibit the characteristic shape memory effect, with predefined geometric and thermomechanical properties. No additional manufacturing or thermal treatment was applied before embedding in the aluminum matrix. The choice of a pre-fabricated component ensured consistency in material performance and transformation behavior throughout this study. The spring has the following dimensions: an outer diameter (D) of 6.0 mm, wire thickness (d) of 0.63 mm, average recovery force of approximately 2.0 N, and a total of 8 active coils (Figure 1).

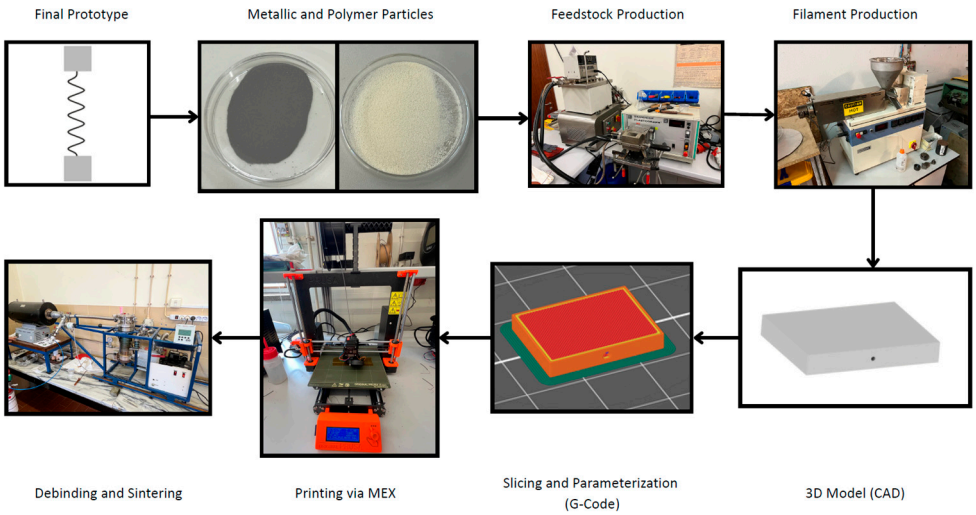


Figure 1. MEX process steps for producing metallic components.

At room temperature (25 °C), the springs are in the martensitic phase, and the Af (final austenite phase transformation) is 69 °C, as confirmed by Differential Scanning Calorimetry (DSC) analysis, reported by Braga et al. (2022) [19].

2.2. Processing

In AM, the MEX process requires additional steps for the fabrication of metal-based components, as illustrated in Figure 1, when compared to the production of polymer parts. These steps include the following: (i) the preparation of the filament composed of metal powder and polymer binder; (ii) the printing of green parts using conventional extrusion-based 3D printing equipment; (iii) a debinding step to remove the organic components from the printed part; and (iv) a final sintering step to densify the metal structure.

The feedstock was prepared by homogenously mixing AlSi7Mg alloy powder (60 wt.%) with the organic binder system. The feedstock was mixed until homogenized in a torque rheometer, using a Plastograph W 50 (Brabender GmbH, Duisburg, Germany) for 45 min at a blade speed of 30 rpm and a temperature of 140 °C. After cooling down, it was granulated into small pellets and sieved at 5 mm. Filaments were made in a single screw extruder (Brabender GmbH & Co., Duisburg, Germany), with 4 heating zones starting at 115 °C with 5 °C increments. In addition, the screw speed was 4 rpm and the nozzle diameter was 1.75 mm.

Subsequently, it was necessary to model the geometry of the specimens using computer-aided design (CAD) software, specifically Inventor Professional 2024 (Autodesk, San Francisco, CA, USA). The resulting 3D model was then processed using PrusaSlicer, where slicing and parameterization were performed to generate the corresponding G-code for AM.

The 3D objects (green part) were printed using a 3D printer, Prusa i3 MK3S (Prusa Research A.S, Prague, Czech Republic). The printing parameters included a nozzle temperature of 160 °C, a bed temperature of 50 °C for the first layer and 60 °C for the remaining ones, an extrusion multiplier in a range from 1.1 to 1.4, a layer height from 0.15 to 0.25 mm, and a printing velocity of 10 mm/s.

To integrate the SMA element, the NiTi wire was manually fitted after production within the printed tight-fit hole, effectively embedding the actuator within the post-sintering aluminum matrix.

2.3. Debinding and Sintering

The debinding and sintering processes were carried out in a single thermal cycle, with heating rates of 1 °C/min up to a maximum temperature of 600 °C. The process was conducted in a tubular furnace under a low-pressure argon atmosphere (4×10^{-2} mbar) for two hours to minimize oxidation. A vacuum-assisted argon environment was selected to limit oxidation during thermal exposure and preserve the surface integrity of the actuators.

2.4. Characterization Techniques

To evaluate the printability of the AlSi7Mg-based metallic filament, a systematic study of key printing parameters was conducted. A factorial design of experiments (DoEs) was implemented to evaluate the influence of three printing parameters on the density of green parts produced via MEX. The parameters analyzed were the extrusion multiplier (1.0 and 1.4), line width (0.5 mm and 0.8 mm), and layer thickness (0.15 mm, 0.20 mm, and 0.25 mm). Small cuboid specimens ($10 \times 10 \times 2$ mm) were printed for each parameter combination, resulting in a total of twelve experimental runs. To quantify the effect of the process parameters on the relative density, a multiple linear regression analysis, supported by ANOVA, was performed.

The printability was assessed through visual inspection for defects (e.g., warping, delamination, and stringing). The dimensional accuracy of the printed and sintered specimens was assessed by measuring dimensions at the top and bottom regions of the parts, comparing the green and sintered states. The three parameters that were evaluated were the thickness (z), length (y), and width (x), using μCT (X-ray micro-computed tomography) with a Bruker SkyScan 1275 (Bruker, Kontich, Belgium). An acceleration voltage of 80 kV and a beam current of 125 μA were set while using a 1 mm aluminum filter and the step-and-shoot mode. The pixel size was set to 10 μm, and the random movement mode was used. In total, 901 projection images were acquired with a 0.4° angular step, with a 5-frame average per step, while using an exposure time of 40 ms. The μCT images were reconstructed with dedicated manufacturer software. Each printed sample was documented and categorized to generate a printability map, facilitating a comparative representation of the performance under different parameter sets. The optimal conditions were then used to fabricate standardized test specimens for all the characterization techniques. Porosity is measured using μCT through the reconstruction and thresholding of the scans. A binary thresholding operation was performed, attributing the color white and black to the part and the non-part (pores), respectively. Afterwards, a shrink wrap operation was performed, effectively working as a definition of the outer shell of the specimen (everything outside this region of interest was disregarded). Finally, the area of each color (white and black) in each slice was calculated, and the density value equals the average of the relation between the area of the white color and the area of the region of interest for the same slice. Pores with a diameter under 8 microns were considered to be the color white and disregarded in the calculation due to equipment limitations.

To analyze the dimensional accuracy and sintering quality, the specimens were μCT scanned, using the same parameters used for the printability analysis. Optical microscopy (OM), with a Leica DM4000 (Wetzlar, Germany), was used to investigate the sintered AlMg7Si matrix quality and the interface region between the matrix and the embedded NiTi spring.

For the proof-of-concept evaluation (Figure 2), a NiTi SMA spring was embedded between two aluminum matrices to simulate a constrained configuration representative of aerospace integration. The initial state corresponded to the spring in its martensitic phase at room temperature (25 °C), allowing deformation under tensile load. After deformation, the system was subjected to thermal activation at approximately 75 °C, activating the austenitic transformation and promoting the complete recovery of the spring's original geometry.

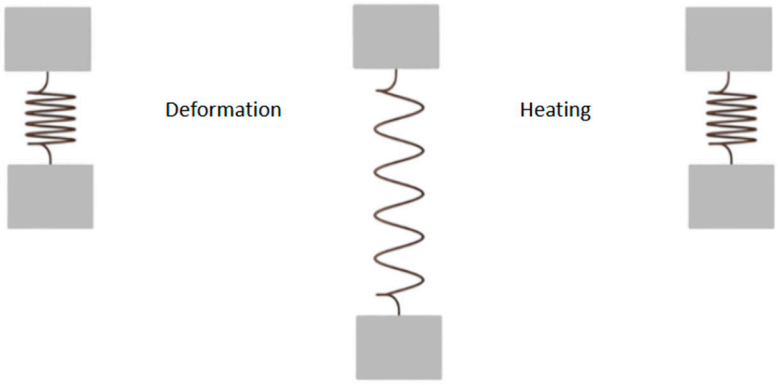


Figure 2. SMA-embedded actuator thermo-mechanical proof of concept.

Tensile tests were carried out at room temperature using a Shimadzu AGS-X universal testing machine (Kyoto, Japan) at a 1 mm/s rate. Upon reaching 20 mm, the displacement was locked, and the specimen was subjected to a thermal stimulus (~75 °C), and a partial recovery was measured, as presented in Figure 2.

3. Results

3.1. Process Optimization via Design of Experiments (DoE)

Since density is a key indicator of internal cohesion and sintering quality in the metal-extruded green parts, maximizing this parameter is essential for achieving structurally sound components [20,21]. Small cuboid specimens (10 × 10 × 2 mm) were produced and analyzed using micro-computed tomography (μCT) to assess porosity. Figure 3 illustrates the effect of parameter optimization, showing the parts before (Figure 3A) and after (Figure 3B) the conforming step. The refined parameter set significantly improved the part quality, leading to homogeneous structures with high geometric accuracy and no discernible internal defects.

Figure 4 illustrates the density outcomes for the different process parameter combinations. Among the three studied variables, layer thickness exhibited the most statistically significant influence on part density (p = 0.019, standardized β = 0.668), followed by the extrusion multiplier (p = 0.046, β = 0.531). The effect of the line width was moderate (β = 0.452), but not statistically significant (p = 0.075), according to the multiple linear regression analysis supported by ANOVA ($F(3,5) = 7.092$, p = 0.030, adjusted R^2 = 0.696).

Higher extrusion multipliers, particularly EM = 1.4, were associated with increased density (Figure 3B), with values reaching up to 99.8%. This behavior is attributed to the enhanced volumetric flow rate, which improves interlayer adhesion and reduces internal voids. Although a slightly higher density (99.9%) was observed with EM = 1.1, LW = 0.8 mm, and Lt = 0.20 mm, this combination had limited replicability. It posed risks

such as material overflow and reduced precision in small features, effects linked to the behavior of the Arachne perimeter generation algorithm [18]. The variation in line width from 0.5 mm to 0.8 mm showed only a marginal effect on density, and, considering the potential trade-offs in geometric fidelity, 0.5 mm was maintained as the standard value.

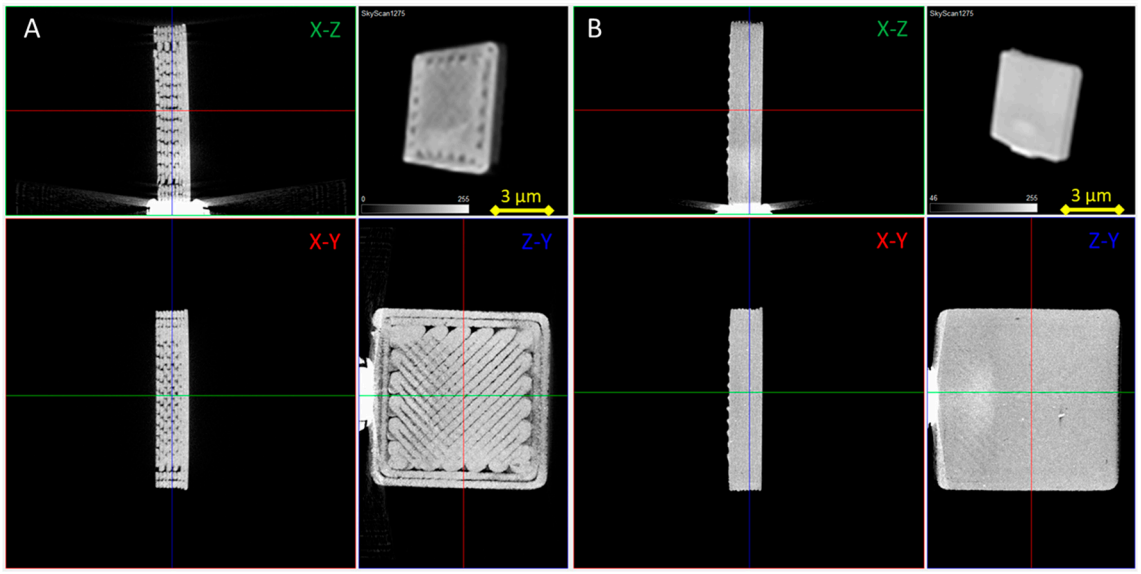
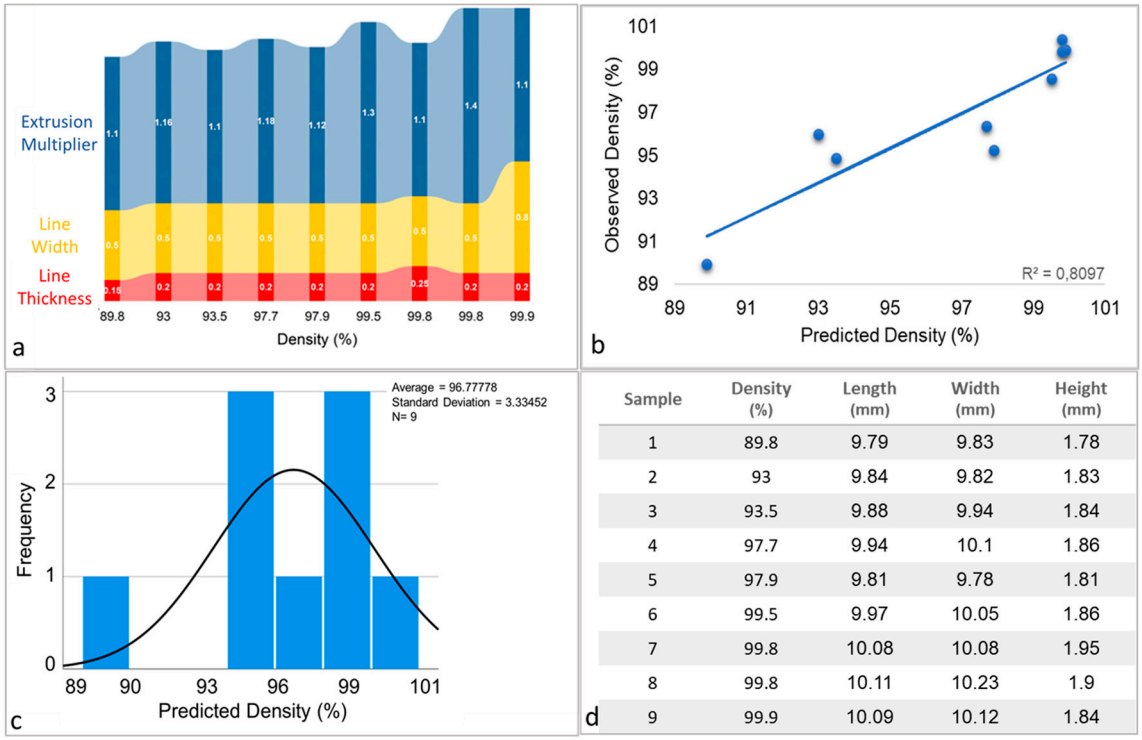


Figure 3. Sample with highest porosity (**A**) and lowest porosity (**B**), calculated via microtomography.



Sample	Density (%)	Length (mm)	Width (mm)	Height (mm)
1	89.8	9.79	9.83	1.78
2	93	9.84	9.82	1.83
3	93.5	9.88	9.94	1.84
4	97.7	9.94	10.1	1.86
5	97.9	9.81	9.78	1.81
6	99.5	9.97	10.05	1.86
7	99.8	10.08	10.08	1.95
8	99.8	10.11	10.23	1.9
9	99.9	10.09	10.12	1.84

d

Figure 4. Density outcomes for the different process parameter combinations: (**a**) the key processing parameters adjustment and their effect on overall density, (**b**) a scatter plot of the observed vs. the predicted density values with a trendline and R^2 = 0.8097, and (**c**) a histogram of the predicted density values with an overlaid normal distribution curve; (**d**) measured dimensions and predicted density of DoE samples.

The layer thickness varied between 0.15 mm and 0.25 mm and had an evident influence on densification. The 0.20 mm setting consistently yielded higher and more reliable

densities. The thinner layers (0.15 mm) tended to cause bonding defects due to insufficient layer deposition, while the thicker layers (0.25 mm) showed acceptable porosity levels but reduced resolution and surface quality. Therefore, 0.20 mm was selected as the optimal compromise between dimensional accuracy and layer fusion.

Although the highest measured density (99.9%) occurred under a different parameter combination, the selected set (EM = 1.4, LW = 0.5 mm, Lt = 0.20 mm) resulted in a comparable density of 99.8%, but with greater statistical confidence and more favorable manufacturing outcomes in terms of repeatability and part resolution.

The multiple linear regression analysis supported by the ANOVA model showed a good fit and predictive power ($F(3,5) = 7.092$, $p = 0.030$), with an adjusted R^2 of 0.696, indicating that approximately 81% of the variance in density is explained by the combination of the layer thickness, line width, and extrusion multiplier.

Additionally, residual analysis confirmed the adequacy of the model, with residuals normally distributed and centered around zero (±3% maximum deviation), as illustrated in Figure 4c. A strong linear correlation was observed between the predicted and measured values (Figure 4b), with $R^2 = 0.8097$, further validating the statistical robustness of the model.

To complement the analysis of the densification, a dimensional evaluation was performed using μCT to assess the geometrical fidelity of the parts relative to the original CAD model. Measurements were carried out for critical features, including the length, width, and height of representative specimens produced with different parameter sets (Figure 4d). For the selected set (EM = 1.4, LW = 0.5 mm, Lt = 0.20 mm), the average deviations were as follows: length = 10.11 ± 0.01 mm, width = 10.23 ± 0.09 mm, and height = 1.9 ± 0.01 mm, compared to the nominal CAD dimensions of 10.00 × 10.00 × 2.00 mm. These values correspond to dimensional deviations below 3.0%, confirming the high fidelity of the printed parts. In contrast, specimens fabricated with extrusion multipliers below 1.2 exhibited larger deviations due to insufficient extrusion effects. These results validate that the selected parameter combination not only optimizes internal density but also ensures geometrical accuracy, reinforcing its suitability for producing functional green parts with minimal post-processing requirements.

The consistency between the statistical predictions and the experimental results highlights the robustness of the selected parameters and confirms their suitability for producing specimens intended for detailed microstructural and mechanical evaluation.

After selecting the optimal printing parameters, a cylindrical specimen with a central through-hole was printed to assess the physical contact between the SMA (NiTi wire) and the green AlSi7Mg matrix. The NiTi wire was manually inserted into the cavity post-printing, and the assembly was subjected to debinding and sintering. Figure 5 shows the cylinder with the embedded wire before (A, B) and after sintering (C), confirming successful integration.

The μCT analysis indicated contact between the wire and surrounding matrix during the green state, with visible deformation around the insertion site, as expected from a tight-fit interference. This mechanical conformity promoted frictional retention and a self-locking effect prior to densification [20]. Post-sintering inspection revealed a continuous aluminum (AA)–SMA interface (Figure 5C, white arrow), with fine geometrical accuracy.

These interfacial features are primarily attributed to the thermal expansion mismatch between the NiTi wire and the aluminum matrix. Additionally, the possible anisotropic shrinkage of the matrix during sintering likely induced radial compressive stresses around the rigid wire. These stresses, concentrated at the interface, promote bonding between the actuator and the sintered matrix, suggesting partial interfacial integrity and the potential for functional mechanical retention under controlled thermal conditions.

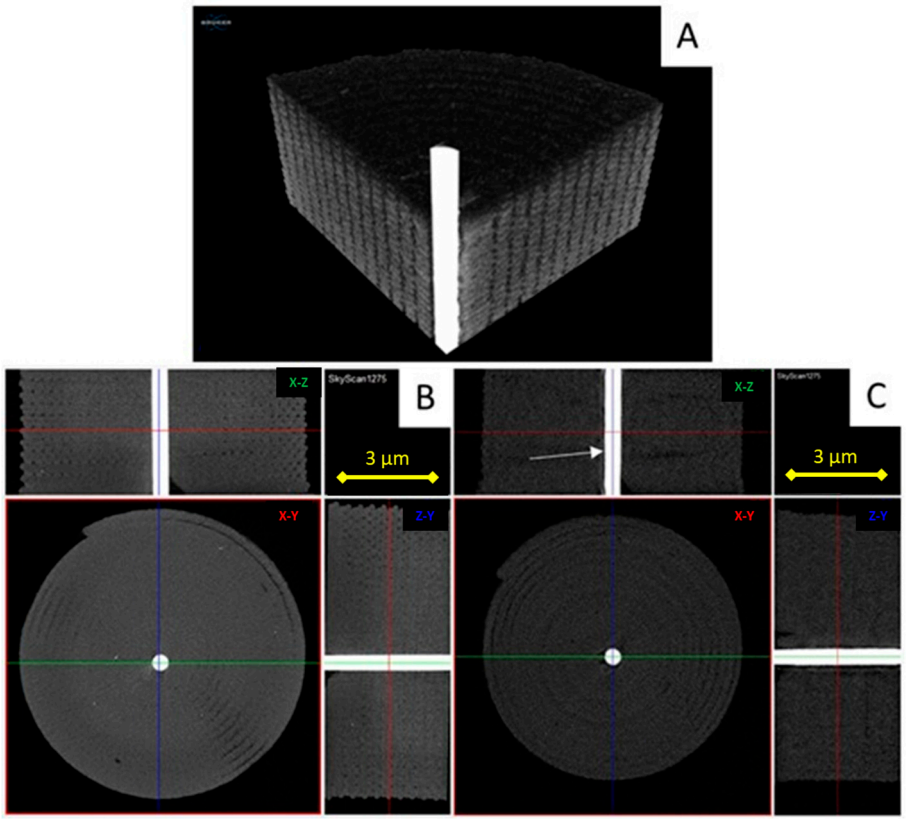


Figure 5. Partial views of the (**A**), (**B**) embedded wire in aluminum in the green part, and (**C**) embedded wire in the sintered part.

3.2. Proof of Concept

Before integrating the NiTi spring, the sinterability of the rectangular geometry was first validated. The specimens with dimensions of 20 × 15 × 3 mm and a central through-hole were printed and subjected to the debinding and sintering cycle. Figure 6A and 6B represent the proof of concept geometry after printing and after sintering, respectively. Post-sintering analysis confirmed that the geometry retained its structural integrity, with minimal warping and high densification. Dimensional evaluation by µCT revealed anisotropic shrinkage (7 to 8% on XY axis and 18% on Z axis), consistent with expected values for sinter-based metal-polymer systems [22]. Few defects, such as delamination or collapse, were observed, indicating that the selected process parameters were sufficient to promote sintering. However, further refinement is necessary to improve the overall part quality. Based on these results, the same geometry and thermal cycle were used to embed the NiTi spring and evaluate the actuator system performance. These results confirm the predictability and consistency of the sintering behavior for the AlMg7Si matrix in this configuration.

To validate a functional proof-of-concept actuator embedded within the aluminum matrix, a NiTi spring was selected as the active element due to its shape memory properties and mechanical responsiveness to thermal stimuli. Building on the previously validated rectangular geometry, a new configuration was adopted to allow the insertion of the spring after shaping and before sintering, while also enabling direct measurement of the recovery force during phase transformation. For this purpose, the same rectangular specimen (20 × 15 × 3 mm) was printed with a central through-hole (Ø 0.8 mm), using the optimized parameters established earlier.

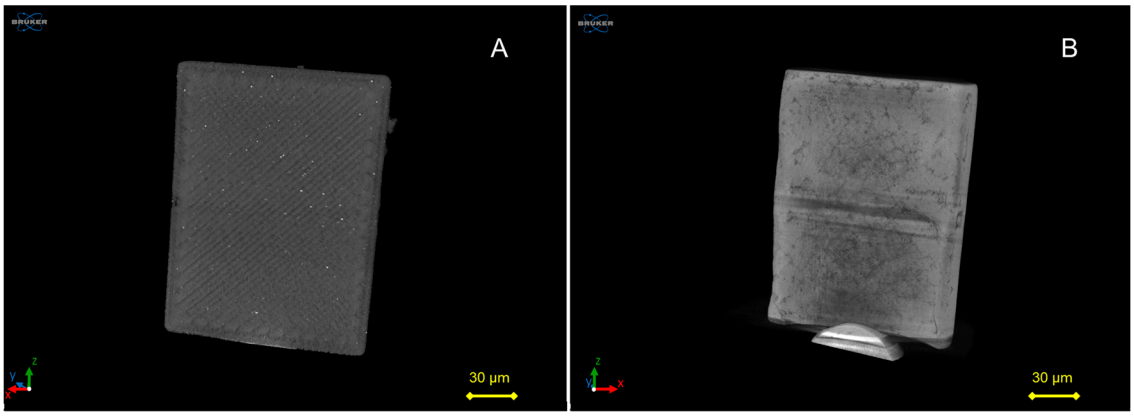


Figure 6. µCT of the aluminum alloy matrix, (**A**) before and (**B**) after sintering.

As shown in Figure 7, all dimensions decreased after sintering, reflecting the expected volumetric shrinkage due to binder removal and particle densification [23,24].

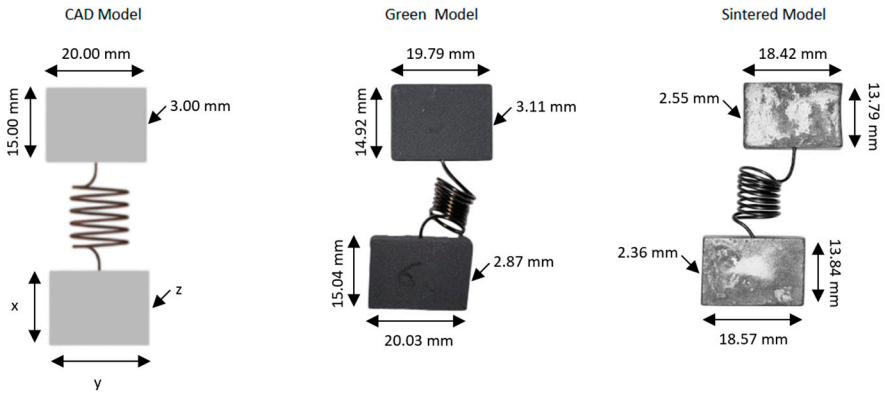


Figure 7. Model, green, and sintered parts with embedded NiTi spring.

Average shrinkage values ranged from 6.92% to 18.01%, with the highest contraction occurring in the thickness direction, (z) =18.01% at the top and 17.77% at the bottom, indicating a more pronounced densification along the build direction. This behavior is consistent with sinter-based MEX processes, where vertical shrinkage is typically more significant due to layer stacking and thermal gradients [25]. The lateral (y) shrinkage was more uniform, with minor variation between the top and bottom sections. The lateral dimension showed a shrinkage of 6.92% (top) and 7.29% (bottom), while the x direction contracted by 7.57% (top) and 7.98% (bottom). The similarity in these values suggests that the part experienced near isotropic shrinkage in the X and Y directions, supporting the overall geometric reproducibility of the process. These results confirm that the selected processing parameters led to predictable and consistent shrinkage, with no evidence of significant asymmetric deformation [24,26]. The minor variations observed between top and bottom regions are attributed to possible differences in local heating and support during sintering.

The important aspect to ensure the functionality of the actuator is the wire matrix interface. Enough adhesion must be ensured so as not to separate the actuator from the matrix. Optical microscopy demonstrates that the matrix was successfully sintered (Figure 8A), suggesting the material's structural integrity. Figure 8B shows a detailed view of the interface between the NiTi wire and the surrounding matrix. The image reveals a coherent interface, with no visible gaps, voids, or delamination between the two materials. The close physical contact and the apparent continuity between the phases suggest that

mechanical tight-fit interlocking was achieved during sintering, even in the absence of strong metallurgical bonding. The absence of large interfacial pores is particularly encouraging, as it supports the mechanical anchoring of the wire and ensures that the actuator can transfer force efficiently to the surrounding matrix during thermal activation. The selected thermal sintering cycle of MEX for the aluminum alloy is shown to be suitable for the SMA actuator, since the maximum temperatures reached did not affect the functional properties, as it was intended. The lower peak temperature applied during the sintering cycle of MEX contributes to maintaining the SMAs' phase composition and microstructure. In this process, there is no driving force for Ni evaporation at ~600 °C, and NiTi retains the Ni content, so its transformation temperatures stay in the intended range. Any precipitates (like Ni_4Ti_3) that control the shape memory behavior can either remain or evolve in a predictable manner, since the heating rate and hold can be tailored [27]. Crucially, the NiTi will not reach temperatures high enough to fully solutionize all precipitates or form undesirable intermetallic phases. Instead, it undergoes a controlled heat treatment, comparable to standard SMA aging protocols (typically 400–600 °C), which are used to optimize functional properties. As a result, the shape memory effect of the alloy can be effectively preserved [27,28]. This shows a novel improved alternative to actuator embedding via metal AM.

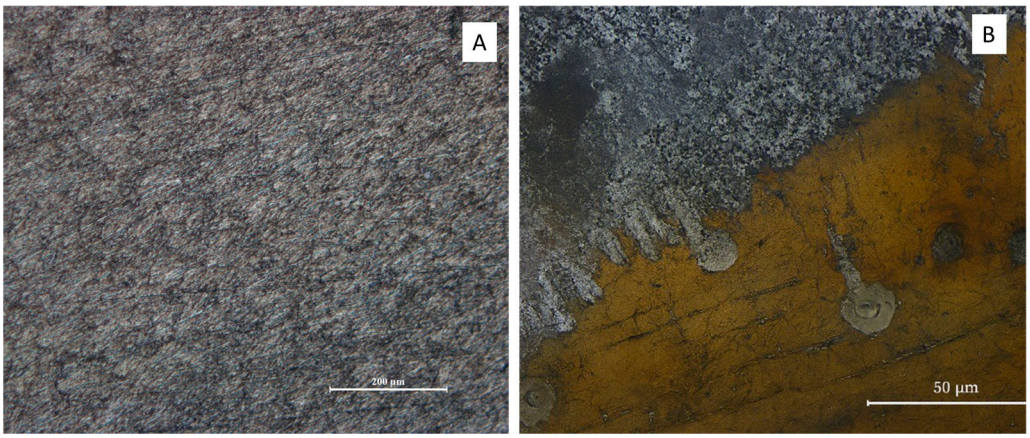


Figure 8. Microscopic images of the (**A**) sintered aluminum matrix and (**B**) the interface bonding between the SMA and the sintered aluminum matrix.

Thermal Actuation Behavior

Figure 9 illustrates the thermo-mechanical response of the sintered rectangular specimen with the SMA spring, subjected to a uniaxial tensile test with thermal activation, which shows elastic behavior until the displacement lock (20 mm). Upon the lock, and before applying heat to the specimen, a decrease in force occurred due to accommodation of the spring, showing an expected asymptotic tendency. After 40 s, heating was applied until the specimen reached 75 °C (sufficient to trigger the austenitic phase transformation of the NiTi spring—A_f = 69 °C), after which the heating source was removed. The spring responded promptly to heating, exhibiting a peak recovery force of 2.25 N, consistent with the literature values for commercial NiTi SMA elements under constrained recovery conditions [19]. This response confirms that the shape memory effect was retained after full processing, including a 600 °C sintering cycle. As the system was cooled naturally, the force gradually decreased, indicating a return to the martensitic phase. This reversible thermal response confirms that the actuator remains functional post-sintering and is capable of repeated transformation cycles within a bonded metallic matrix.

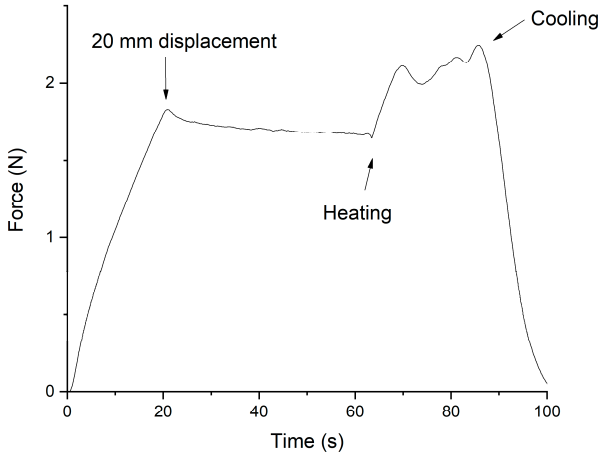


Figure 9. Proof-of-concept tensile test.

To analyze the actuation behavior, a heating–cooling sequence was repeated over three full cycles, as shown in Figure 10. A progressive decrease in peak force was observed, from 2.25 N in the first cycle to 1.82 N in the third, although the response remained symmetric and reproducible throughout. This degradation is characteristic of thermomechanical cycling in NiTi-based actuators and is particularly pronounced when the wire is embedded in a constraining matrix. The reduction in actuation force is primarily attributed to internal stress accumulation, interfacial friction, and partial stabilization in the martensitic phase, which can make a complete reversal transformation to austenite [12].

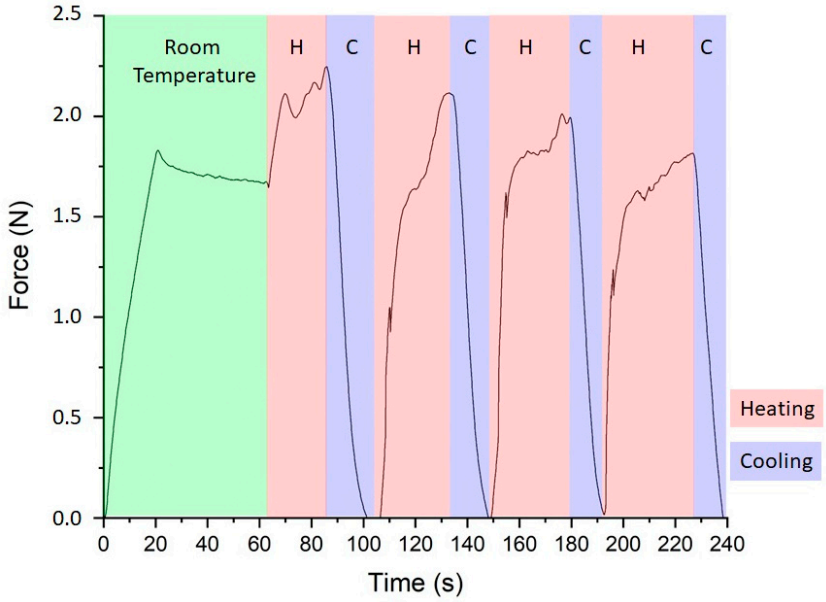


Figure 10. Proof-of-concept thermo-mechanical cycle.

Such effects are well-documented and typically stabilize after a few cycles, as the material enters a steady-state actuation regime [29]. To mitigate this behavior, strategies such as preconditioning (training) the SMA wire before embedding [30], applying surface coatings to reduce friction [31], or optimizing matrix geometry to minimize mechanical constraints can be considered for future implementations [29].

Nonetheless, the tensile test confirmed the two core objectives of this study: the NiTi spring maintained its shape memory effect after a 600 °C heat treatment, and there was no detachment of the wire from the matrix for these windows of force and displacement.

This confirms that the mechanical embedding method, supported by sintering-induced shrinkage and bonding, provided sufficient interfacial retention to support actuator function under load.

These results demonstrate that reliable and reversible actuation is achievable in sintered aluminum matrices containing embedded NiTi springs. The system exhibited both functional recovery and structural stability, validating the feasibility of integrating NiTi-based actuators into sintered metallic components. This behavior confirms the preservation of the shape memory effect after integration and heat treatment, supporting the potential application of NiTi elements as embedded actuators in metallic aerospace structures.

4. Challenges and Opportunities for SMA-AA Integration in Aerospace Components

The integration of SMAs, particularly NiTi, into aluminum matrices produced via sinter-based MEX presents both exciting opportunities and critical challenges for aerospace applications. One of the main challenges lies in the inherent thermal expansion mismatch between NiTi and aluminum. During sintering and thermal activation, this mismatch can generate residual stresses at the interface, often leading to localized delamination, cracking, or distortion in the matrix surrounding the wire. These effects are particularly pronounced during the martensitic–austenitic phase transformation of the SMA, which induces dimensional recovery while the surrounding matrix restricts its motion [32].

Additionally, the bonding mechanism at the interface is predominantly mechanical, especially when diffusion is limited by processing conditions such as relatively low sintering temperatures for aluminum. The successful integration of SMA elements within metallic matrices enables the creation of lightweight, multifunctional components capable of actuation, self-adaptation, and vibration damping, without relying on traditional hinges or motors. This furthers the development of fully embedded deployment systems in nanosatellites, adaptive structures, or thermally responsive surfaces for reconfigurable aerospace components [33].

Looking forward, there are several promising research directions to overcome the identified limitations. These include applying localized surface treatments to improve bonding, developing optimized sintering profiles tailored to hybrid systems, and understanding how other treatments, such as anodizing, affect the overall performance of the system. Numerical modeling and the in situ monitoring of thermo-mechanical behavior during sintering could also contribute to the adoption of SMA–AA systems in aerospace design.

5. Conclusions

This study successfully demonstrated the integration of SMA (NiTi) actuators into an aluminum matrix (AlSi7Mg) using a sinter-based material extrusion additive manufacturing approach. The methodology combined filament fabrication, 3D printing, and sintering in a single workflow, enabling the co-processing of structural and functional elements.

Micro-computed tomography and tensile testing revealed strong interfacial bonding between the NiTi wires and the aluminum matrix, with no evidence of delamination or detachment during mechanical loading. The sintered specimens exhibited controlled shrinkage (~18% along the *z*-axis), consistent with the densification behavior observed in metal-filled MEX systems, validating the process viability for consolidated green parts.

Notably, the embedded NiTi elements retained their functional shape memory effect after the 600 °C sintering cycle, demonstrating reversible actuation across multiple thermal cycles. This confirms that the functional behavior is preserved despite thermal exposure and mechanical constraints imposed by the matrix.

The optimization of printing parameters using a design of experiments approach contributed to achieving high green part density (up to 99.9%), reduced porosity, and dimensional accuracy, which are factors critical for successful sintering and actuator integration.

These results establish a solid framework for developing lightweight, multifunctional aerospace components that combine structural performance with active actuation. The one-step integration of actuator and matrix materials reduces assembly complexity, improves reliability, and opens opportunities for applications such as morphing structures, embedded sensing, or self-healing systems in demanding environments.

Future work should focus on cyclic durability, fatigue behavior, and integration of multiple actuators to explore programmable deformation modes and control strategies for embedded smart systems.

Author Contributions: Conceptualization, B.A. and P.F.R.; methodology, B.A. and R.S.; validation, P.F.R. and D.G.; formal analysis, B.A., R.S. and R.C.; investigation, G.O. and L.C.; data curation, B.A., R.C., R.T. and D.G.; writing—original draft preparation, B.A.; writing—review and editing, D.G. and P.F.R.; visualization, B.A. and R.T.; supervision, P.F.R. All authors have read and agreed to the published version of the manuscript.

Funding: This research received no external funding.

Data Availability Statement: Data is contained within the article.

Acknowledgments: This work was carried out within the framework of the "Agendas para a Inovação Empresarial" (Project no 49, acronym "INOV.AM", with reference PRR/49/INOV.AM/EE, operation code 02/C05 i01.01/2022.PC644865234-00000004), supported by the RRP Recovery and Resilience Plan and by the European Funds NextGeneration EU. http://www.recuperarportugal.gov.pt/. This research was sponsored by national funds through the FCT—Fundação para a Ciência e a Tecnologia, under the projects UID/00285—Centre for Mechanical Engineering, Materials and Processes, LA/P/0112/2020, and grant UI/BD/154813/2023. CAPES-NOVAÇÃO 99999.011943/2013-00-23038.002572/2024-87.

Conflicts of Interest: The authors declare no conflicts of interest.

References

1. Blakey-Milner, B.; Gradl, P.; Snedden, G.; Brooks, M.; Pitot, J.; Lopez, E.; Leary, M.; Berto, F.; du Plessis, A. Metal Additive Manufacturing in Aerospace: A Review. *Mater. Des.* **2021**, *209*, 110008. [CrossRef]
2. Capovilla, G.; Cestino, E.; Reyneri, L. Modular Multifunctional Composite Structure for CubeSat Applications: Embedded Battery Prototype Modal Analysis. *Aerospace* **2023**, *10*, 1009. [CrossRef]
3. Kim, T.-H.; Alzaabi, A.; Suh, J.-E.; Han, J.-H. A Unit-Separable Earth Observation CubeSat Structure Concept Using Flat-Retractable Truss Structure. In *Proceedings of the Active and Passive Smart Structures and Integrated Systems XVI*; Han, J.-H., Shahab, S., Yang, J., Eds.; SPIE: Long Beach, CA, USA, 2022; p. 75. [CrossRef]
4. Lieberwirth, C.; Harder, A.; Seitz, H. Extrusion Based Additive Manufacturing of Metal Parts. *J. Mech. Eng. Autom.* **2017**, *7*, 79–83. [CrossRef]
5. Alves, B.; Gatões, D.; Soares, P.; Rodrigues, L.; Vieira, M.T. Material Extrusion: Shaping and Sintering Optimization Through µ-Tomography. In *Proceedings of the Euro PM2023 Proceedings*; EPMA: Lisbon, Portugal, 2023. [CrossRef]
6. Silva Cerejo, F.; Gatões, D.; Vieira, T. Optimization of Metallic Powder Filaments for Additive Manufacturing Extrusion (MEX). *Int. J. Adv. Manuf. Technol.* **2021**, *115*, 2449–2464. [CrossRef]
7. Santos, C.; Gatões, D.; Cerejo, F.; Vieira, M.T. Influence of Metallic Powder Characteristics on Extruded Feedstock Performance for Indirect Additive Manufacturing. *Materials* **2021**, *14*, 7136. [CrossRef] [PubMed]
8. Hoffmann, M.; Elwany, A. Material Extrusion Additive Manufacturing of AISI 316L Pastes. *J. Manuf. Process* **2023**, *108*, 238–251. [CrossRef]
9. Presciutti, A.; Gebennini, E.; Liberti, F.; Nanni, F.; Bragaglia, M. Comparative Life Cycle Assessment of SLS and MFFF Additive Manufacturing Techniques for the Production of a Metal Specimen. *Materials* **2023**, *17*, 78. [CrossRef]
10. Braz Fernandes, F.M.; Camacho, E.; Rodrigues, P.F.; Inácio, P.; Santos, T.G.; Schell, N. In Situ Structural Characterization of Functionally Graded Ni–Ti Shape Memory Alloy During Tensile Loading. *Shape Mem. Superelasticity* **2019**, *5*, 457–467. [CrossRef]

11. Lima, P.C.; Rodrigues, P.F.; Ramos, A.S.; da Costa, J.D.M.; Braz Fernandes, F.M.; Vieira, M.T. Experimental Analysis of NiTi Alloy during Strain-Controlled Low-Cycle Fatigue. *Materials* **2021**, *14*, 4455. [CrossRef]
12. Zhao, T.; Kang, G.; Yu, C.; Kan, Q. Experimental Investigation of the Cyclic Degradation of the One-Way Shape Memory Effect of NiTi Alloys. *Int. J. Miner. Metall. Mater.* **2019**, *26*, 1539–1550. [CrossRef]
13. Liu, Q.; Feng, Y.; Liu, B.; Xie, Q.; Zhou, J.; Zhang, G. Regulation of Microstructure, Phase Transformation Behavior, and Enhanced High Superelastic Cycling Stability in Laser Direct Energy Deposition NiTi Shape Memory Alloys via Aging Treatment. *Mater. Sci. Eng. A* **2024**, *915*, 147207. [CrossRef]
14. Rodrigues, P.F.; Fernandes, F.M.B.; Magalhães, R.; Camacho, E.; Lopes, A.; Paula, A.S.; Basu, R.; Schell, N. Thermo-Mechanical Characterization of NiTi Orthodontic Archwires with Graded Actuating Forces. *J. Mech. Behav. Biomed. Mater.* **2020**, *107*, 103747. [CrossRef]
15. Carnier, F. Deployment of a CubeSat Radiative Surface through an Autonomous Torsional SMA Actuator. *Mater. Res. Proc.* **2023**, *37*, 413–416.
16. Boschetto, A.; Bottini, L.; Costanza, G.; Tata, M.E. Shape Memory Activated Self-Deployable Solar Sails: Small-Scale Prototypes Manufacturing and Planarity Analysis by 3D Laser Scanner. *Actuators* **2019**, *8*, 38. [CrossRef]
17. Huang, G.Q.; Yan, Y.F.; Wu, J.; Shen, Y.F.; Gerlich, A.P. Microstructure and Mechanical Properties of Fine-Grained Aluminum Matrix Composite Reinforced with Nitinol Shape Memory Alloy Particulates Produced by Underwater Friction Stir Processing. *J. Alloys Compd.* **2019**, *786*, 257–271. [CrossRef]
18. Loong, T.T.; Jamian, S.; Ismail, A.E.; Muhd Nur, N.H.; Watanabe, Y. Residual Stresses in Shape Memory Alloy Fiber Reinforced Aluminium Matrix Composite. *IOP Conf. Ser. Mater. Sci. Eng.* **2017**, *165*, 012002. [CrossRef]
19. Braga, R.; Rodrigues, P.F.; Cordeiro, H.; Carreira, P.; Vieira, M.T. The Study of New NiTi Actuators to Reinforce the Wing Movement of Aircraft Systems. *Materials* **2022**, *15*, 4787. [CrossRef]
20. Inverarity, S.; Das, R.; Mouritz, A. Composite-to-Metal Joining Using Interference Fit Micropins. *Compos. Part A Appl. Sci. Manuf.* **2022**, *156*, 106895. [CrossRef]
21. Kuipers, T.; Doubrovski, E.L.; Wu, J.; Wang, C.C.L. A Framework for Adaptive Width Control of Dense Contour-Parallel Toolpaths in Fused Deposition Modeling. *Comput.-Aided Des.* **2020**, *128*, 102907. [CrossRef]
22. Ghamarian, I.; Ball, S.; Ghayoor, M.; Pasebani, S.; Tabei, A. Statistical Analysis of Spatial Distribution of Pores in Metal Additive Manufacturing. *Addit. Manuf.* **2021**, *47*, 102264. [CrossRef]
23. Jimbo, K.; Tateno, T. Shape Contraction in Sintering of 3D Objects Fabricated via Metal Material Extrusion in Additive Manufacturing. *Int. J. Autom. Technol.* **2019**, *13*, 354–360. [CrossRef]
24. Pellegrini, A.; Guerra, M.G.; Lavecchia, F. Shrinkage Evaluation and Geometric Accuracy Assessment on 17–4 PH Samples Made by Material Extrusion Additive Manufacturing. *J. Manuf. Process* **2024**, *109*, 394–406. [CrossRef]
25. Gatões, D.; Cacho, L.; Vieira, M.T. μCT Non-destructive Testing Of Additively Manufactured 3Dobjects As Support For True Sustainability. In Proceedings of the Euro Powder Metallurgy 2023 Congress & Exhibition, Lisbon, Portugal, 1–4 October 2023. [CrossRef]
26. Liu, Y.; Jiang, D.; Ning, F. Sintering Mechanisms in Metal Extrusion-Based Sintering-Assisted Additive Manufacturing: State-of-the-Art and Perspectives. *J. Manuf. Sci. Eng.* **2025**, *147*, 070801. [CrossRef]
27. Otsuka, K.; Ren, X. Physical Metallurgy of Ti-Ni-Based Shape Memory Alloys. *Prog. Mater. Sci.* **2005**, *50*, 511–678. [CrossRef]
28. Freitas Rodrigues, P.; Reshie, H.; de Sousa, T.G.; Paula, A. dos S.; Braz Fernandes, F.M.; Basu, R. Controlling the Phase Transformation Window during Stages of Hot/Cold Forging of Ni-Rich Ni–Ti Alloy. *J. Mater. Res. Technol.* **2021**, *15*, 3784–3794. [CrossRef]
29. Lagoudas, D.C. *Shape Memory Alloys: Modeling and Engineering Applications*; Springer: New York, NY, USA, 2008; ISBN 9780387476841.
30. Jani, J.M.; Leary, M.; Subic, A.; Gibson, M.A. A Review of Shape Memory Alloy Research, Applications and Opportunities. *Mater. Des.* **2015**, *56*, 1078–1113. [CrossRef]
31. Payandeh, Y.; Meraghni, F.; Patoor, E.; Eberhardt, A. Debonding Initiation in a NiTi Shape Memory Wire–Epoxy Matrix Composite. Influence of Martensitic Transformation. *Mater. Des.* **2010**, *31*, 1077–1084. [CrossRef]
32. Farvizi, M.; Bahamirian, M.; Faraji, A.; Kim, H.S. Influence of Ceramic Reinforcement Characteristics on the Microstructure and Wear Behavior of NiTi Matrix Composites. *Materialia* **2023**, *28*, 101726. [CrossRef]
33. Rodinò, S.; Maletta, C. Multiphysics Modeling and Optimization of an Innovative Shape Memory Alloy-Polymer Active Composite. *Polymer* **2024**, *307*, 127316. [CrossRef]

Disclaimer/Publisher's Note: The statements, opinions and data contained in all publications are solely those of the individual author(s) and contributor(s) and not of MDPI and/or the editor(s). MDPI and/or the editor(s) disclaim responsibility for any injury to people or property resulting from any ideas, methods, instructions or products referred to in the content.